Solar Physics
DOI: 10.1007/•••••-•••-•••-••••-•

HELIOSEISMOLOGY OF SUNSPOTS: CONFRONTING OBSERVATIONS WITH THREE-DIMENSIONAL MHD SIMULATIONS OF WAVE PROPAGATION

R. CAMERON[1] · **L. GIZON**[1] · **T. L. DUVALL Jr.**[2]

Received ; accepted

Abstract The propagation of solar waves through the sunspot of AR9787 is observed using temporal cross-correlations of SOHO/MDI Dopplergrams. Because the interaction of solar waves with the magnetic field is strong near the solar surface, the interpretation of the observations requires numerical modeling. We use three-dimensional MHD numerical simulations to compute the propagation of wave packets through self-similar magneto-hydrostatic sunspot models. We find that the simulation and the f-mode observations are in good agreement when the model sunspot has a peak field strength of 3 kG at the photosphere, less so for lower field strengths. Constraining the sunspot model with helioseismology is only possible because the direct effect of the magnetic field on the waves has been fully taken into account. Our work shows that the full-waveform modeling of sunspots is feasible.

Keywords: Sun: Helioseismology, Sun: sunspots, Sun: magnetic fields

1. Introduction

The subsurface magnetic structure of sunspots is poorly known. The theoretical picture is that sunspots are either monolithic or not (Parker, 1979), or change from being monolithic to "disconnected" over the course of the first few days of their lives (Schüssler and Rempel, 2005). The observational picture is limited because the subsurface structure is inherently difficult to infer. The most promising possibility by far is local helioseismology. For example the time-distance approach (Duvall et al., 1993) has been applied to determine wave-speed variations and flows associated with sunspots (e.g. Kosovichev, Duvall,

[1] Max-Planck-Institut für Sonnensystemforschung, 37191 Katlenburg-Lindau, Germany
[2] Solar Physics Laboratory, NASA Goddard Space Flight Center, Greenbelt, MD 20771, USA

and Scherrer, 2000; Zhao, Kosovichev and Duvall, 2001; Couvidat, Birch and Kosovichev, 2006). Most inversions to date, however, have ignored the direct effects of the magnetic field on waves and the fact that sunspot perturbations, such as the Wilson depression, are not weak near the solar surface (first-order perturbation theory does not apply there). An exception is the work of Crouch et al. (2005) who constructed simplified sunspot models that were capable of reproducing the phase shifts and attenuation coefficients observed by Braun (1995), while properly treating the magnetoacoustic mode conversion. The effect of sunspots on waves has also been observationally explored using other local-helioseismology tools such as helioseismic holography (Lindsey and Braun, 1997; Braun and Lindsey, 1997), which suggest that near-surface magnetic effects are very important.

The physical principles relevant to the propagation of waves through magnetic concentrations have been elucidated in various studies in two dimensions (for example Bogdan et al., 1996; Cally and Bogdan, 1997; Cally, 2007). Three-dimensional simulations provide an opportunity to not only learn more about the physics of wave propagation in magnetized atmospheres, but also through a direct comparison with observations to learn more about sunspots. The latter goal is the the motivation of this paper.

SOHO/MDI observations of sunspot AR9787 are presented in Section 2 and their helioseismic analysis in Section 3. We describe our numerical simulation code in Section 4. The comparison between the observations and the simulations is very encouraging, as shown in Section 5. We place a helioseismic constraint on the sunspot magnetic field in Section 6. Our work strongly suggests that we will be able to use observations and simulations in combination to constrain the subsurface structure of sunspots by taking direct and indirect magnetic effects into account.

2. SOHO/MDI observations of Active Region 9787

The helioseismic analysis of a sunspot is more or less difficult depending on which sunspot is being studied. We have been searching the SOHO/MDI database for the ideal sunspot, i.e. a sunspot which is isolated (does not belong to a complex sunspot group), has a simple geometry (circular shape), and evolves slowly in time as it moves across the solar disk. In order to find such a "theorist's sunspot", we searched the MDI Dynamics Program which combines the advantage of a good spatial resolution (0.12° at disk center) with a complete view of the solar disk. The full-disk Dopplergrams are available each minute during two to three months each year since 1996. The sunspot we have selected is that of Active Region 9787, continuously observed by MDI during 9 days on 20-28 January 2002. The Dopplergrams were remapped using Postel's azimuthal equidistant projection almost –but not exactly– centered on the sunspot, using a tracking angular velocity of -0.1102° day^{-1} (in the Carrington frame). In addition to the Dopplergrams, we also used the line-of-sight magnetograms (each minute) and all the intensity images (one per 6 hr). The daily averages of these three quantities are shown in Figure 1. Apart from some plage, there is no other active

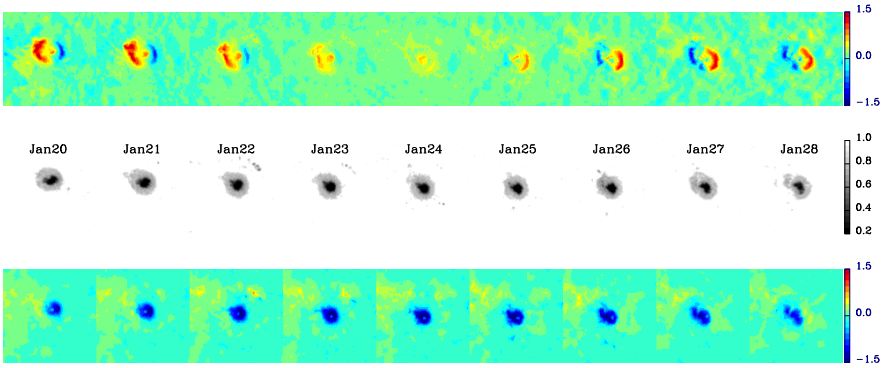

Figure 1. SOHO/MDI observations of the sunspot of Active Region 9787 during the period 20-28 January 2002. Shown are the daily averages of the line-of-sight Doppler velocity (top row), the intensity (middle row), and the line-of-sight magnetic field (bottom row). The color bars are in units of km/s, relative intensity, and kG, from top to bottom.

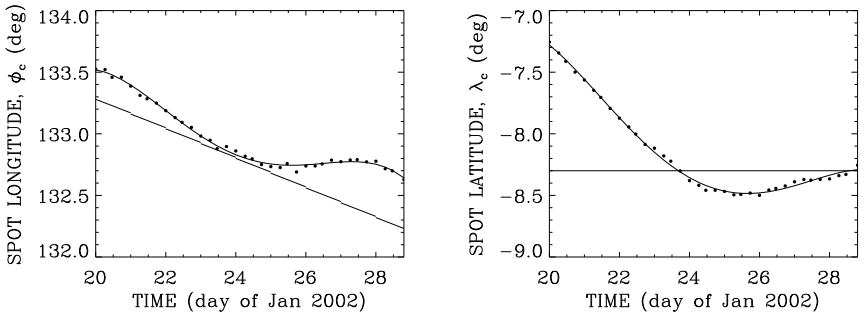

Figure 2. Coordinates of the center of the sunspot's umbra as a function of time. Left: Carrington longitude of the umbra (dots) and Carrington longitude at the center of the Postel projection (line segments). Right: Latitude of the umbra (dots) and latitude at the center of the Postel projection (horizontal line).

region in the vicinity of the sunspot during the entire observation sequence. The sunspot of AR9787 is large and quite stable over the 9 days of the observations, even though it starts decaying from January 27 onward.

Using the MDI intensity images, we measured the center of the sunspot's umbra. As shown in Figure 2, the sunspot has a significant amount of proper motion. Thus we chose to split the time series into 6-hr subsets and to analyze each subset separately. The images belonging to each particular subset were remapped into a new Postel map, with the center of the projection corresponding exactly to the center of the sunspot's umbra in the middle of the 6-hr time interval. These 36 6-hr time series of Dopplergrams, centered on the sunspot's position, are the basic data that we used for the helioseismic analysis, which we discuss in the next section.

The average intensity image of the sunspot, corrected for the proper motion of the sunspot, is shown in Figure 3. From this average image, which is still

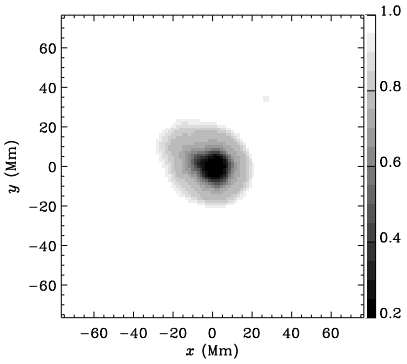

Figure 3. SOHO/MDI intensity image of AR 9787 averaged over 9 days, after correcting for the proper motion of the sunspot. The intensity is measured relatively to the quiet-Sun value.

sharp, we determine the average umbral and penumbral radii to be 9 Mm and 20 Mm respectively.

3. Observed f-mode cross-covariance function

We study sunspot AR9787 using cross-covariances of the random wavefield, as is done in time-distance helioseismology (Duvall et al. 1993). The temporal cross-covariance between two points on the solar surface provides information about the Green's function between these two points. This interpretation has recently been shown to be correct in the case of homogeneously distributed random sources in an arbitrarily complex medium (Colin de Verdière 2006, Gouédard et al. 2007).

In this paper, and for the sake of simplicity, we wish to observe the propagation of f modes through the sunspot. Thus we filter the Dopplergrams in 3D Fourier space to only keep the f modes. Let us denote by $\phi(\boldsymbol{r},t)$ the filtered Doppler velocity, where $\boldsymbol{r}$ is a position vector and t is time. Rather than studying the cross-covariance of ϕ between two spatial points, we consider the cross-covariance between ϕ averaged over a great circle Γ, denoted by $\overline{\phi}(\Gamma,t)$, and ϕ measured at any other point $\mathbf{r}$:

$$C(\boldsymbol{r},t)=\int_0^T \overline{\phi}(\Gamma,t')\phi(\boldsymbol{r},t+t')\,dt', \tag{1}$$

where the effective integration time is $T=9$ days, or 36 times 6 hours. Since averaging ϕ over Γ is equivalent to selecting only the horizontal wavevectors that are perpendicular to Γ, the above cross-covariance function gives us information about plane wave packets that propagate away from Γ. In simple words, the cross-covariance at time lag t tells us about the position of a wave packet, a time t after it has left Γ. In the rest of the paper we fix the distance between Γ and

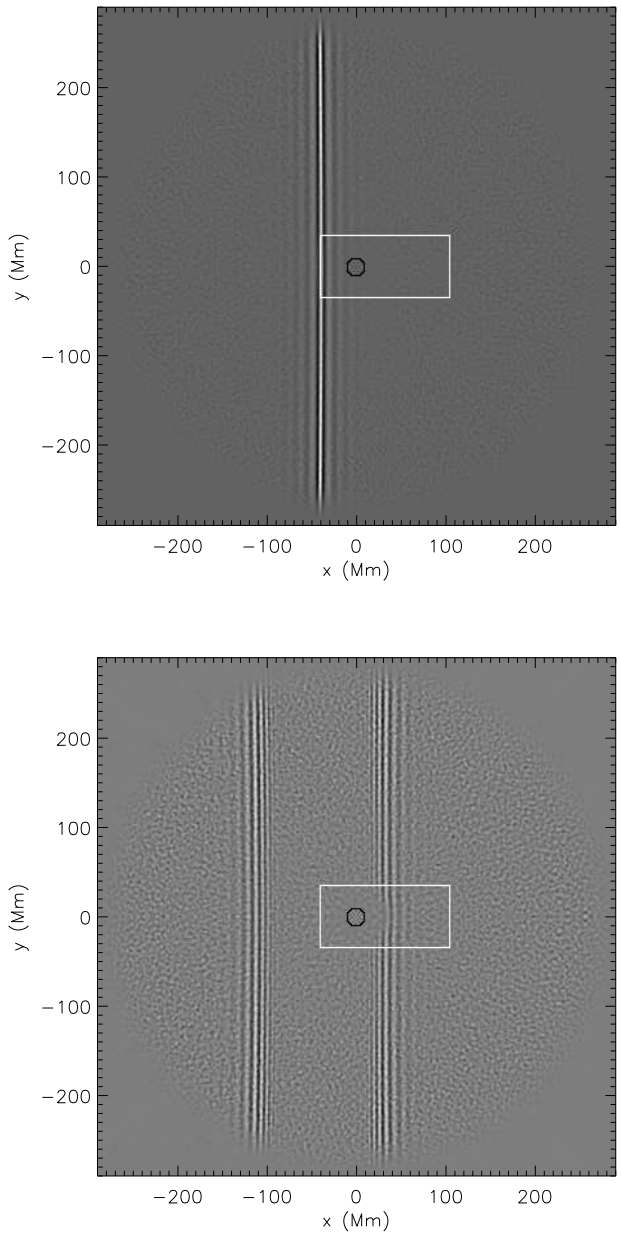

Figure 4. The upper panel shows the observed f-mode MDI cross-covariance function at zero time lag. The sunspot (black circle) is at the center of the Postel map, a distance $\Delta = 40$ Mm from the meridian Γ (white). The lower panel shows the same cross-covariance at time lag $t = 130$ min. In order to increase the signal to noise ratio, the cross-covariance was averaged over all wave directions. It is easy to see, by eye, that the waves are affected by their passage through the sunspot. The white rectangles show the size of the simulation box.

the center of the sunspot at $\Delta = 40$ Mm. Since $\Delta \gg \lambda$, where $\lambda \sim 5$ Mm is the dominant wavelength, the sunspot is in the far field of Γ.

For any particular choice of orientation of Γ, the computed cross-covariance is very noisy. Thus the need for some spatial averaging. Let us pick a reference great circle coincident with the meridian at a distance 40 Mm eastward of the center of the sunspot. Because sunspot AR 9787 is almost invariant by rotation around its center, we can compute many equivalent cross-covariance functions corresponding to many different directions of the incoming wavepacket, derotate these about the center of the sunspot so that they match the reference cross-covariance, and average them to take the noise down. We have performed this averaging over all the directions of the incoming wavevectors, with a fine sampling of 1 degree. As seen in Figure 4, this enables us to reach a very good signal-to-noise level.

4. Three-dimensional MHD simulation of wave propagation through a sunspot

4.1. The equations

We use the ideal MHD equations linearized about an arbitrary inhomogeneous, magnetized atmosphere. We assume a local cartesian geometry defined by horizontal coordinates x and y and the vertical coordinate z increases upwards. The level $z = 0$ is assumed to correspond to the photosphere, as defined in model S (Christensen-Dalsgaard et al., 1996). Under the assumptions that gravitational acceleration, g, is constant and that there is no background steady flow, the equation governing the wave-induced displacement vector $\boldsymbol{\xi}$ is (e.g. Cameron, Gizon, and Daiffallah, 2007)

$$\rho_0 \partial_t^2 \boldsymbol{\xi} = \boldsymbol{F}', \tag{2}$$

where

$$\boldsymbol{F}' = -\boldsymbol{\nabla} P' + \rho' g \hat{\boldsymbol{z}} + \frac{1}{4\pi}(\boldsymbol{J}' \times \boldsymbol{B}_0 + \boldsymbol{J}_0 \times \boldsymbol{B}') \tag{3}$$

is the linearized force acting on a fluid element (first order in $\boldsymbol{\xi}$). In this paper the subscript 0 variables represent the steady inhomogeneous background atmosphere and the primed quantities represent the wave-induced perturbations. In the above equation, the density, pressure, magnetic field and electric current are denoted by the symbols ρ, P, $\boldsymbol{B}$ and $\boldsymbol{J}$ respectively. The system is closed by the following relations that define $\boldsymbol{F}'$ in terms of $\boldsymbol{\xi}$:

$$\rho' = -\boldsymbol{\nabla} \cdot (\rho_0 \boldsymbol{\xi}), \tag{4}$$

$$P' = c_0^2(\rho' + \boldsymbol{\xi} \cdot \boldsymbol{\nabla} \rho_0) - \boldsymbol{\xi} \cdot \boldsymbol{\nabla} P_0, \tag{5}$$

$$\boldsymbol{B}' = \boldsymbol{\nabla} \times (\boldsymbol{\xi} \times \boldsymbol{B}_0), \tag{6}$$

$$\boldsymbol{J}' = \boldsymbol{\nabla} \times \boldsymbol{B}', \tag{7}$$

where c_0 is the background sound speed.

Whilst we have employed ideal MHD, the waves on the Sun are strongly attenuated, presumably as a result of scattering off the time-dependent granulation. Empirically, a solar mode with horizontal wavevector $\boldsymbol{k}$ decays like $e^{-\gamma_k t}$ where $1/\gamma_k$ is the e-folding lifetime at wavenumber $k = \|\boldsymbol{k}\|$. Introducing $\boldsymbol{v}'$ as the wave velocity, for each horizontal Fourier mode we write

$$\rho_0(\partial_t + \gamma_k)\boldsymbol{v}'(\boldsymbol{k}, z, t) = \boldsymbol{F}'(\boldsymbol{k}, z, t), \tag{8}$$

$$(\partial_t + \gamma_k)\boldsymbol{\xi}(\boldsymbol{k}, z, t) = \boldsymbol{v}'(\boldsymbol{k}, z, t). \tag{9}$$

In the above equations, any function $f(\boldsymbol{k}, z, t)$ refers to the spatial Fourier transform of $f(x, y, z, t)$. For $\gamma_k > 0$ the system is damped. The eigenstates, pairs of $(\boldsymbol{\xi}, \boldsymbol{v}')$, are independent of γ_k, although the eigenvalues are naturally affected. This is the advantage of this approach. The attenuation that we have implemented acts only in the time domain and is suitable for our purpose, although in the Sun attenuation is more complicated. An alternate way of introducing this phenomenological time attenuation would have been to perform the ideal calculation and then impose the decay in the time domain post-facto after the calculation has ended.

In this paper we focus on the f modes (solar-surface gravity waves), for which the attenuation has been measured to be

$$\gamma_k = \gamma_* \left(k/k_*\right)^{2.2}, \tag{10}$$

where $\gamma_*/\pi = 100$ μHz and $k_* = 902/R_\odot$ is a reference wavenumber (Duvall, Kosovichev and Murawski, 1998; Gizon and Birch, 2002).

4.2. The code

We use a modified version of the SLiM code which is, apart from the modifications discussed below, described in Cameron, Gizon, and Daiffallah (2007). The code has been tested against analytic solutions - some of these tests are also described in detail in Cameron, Gizon, and Daiffallah (2007).

The present code includes two 'sponge' layers at the top and the bottom of the box. In the top layer above the temperature minimum we heavily damp the waves and systematically reduce the effect of the Lorentz force. This layer only affects waves which have escaped through the photosphere. Likewise the bottom layer damps the waves that propagate downwards. The purpose of both layers is to minimize the effects of the boundaries which would otherwise artificially reflect the waves.

An additional change has been to introduce the mode attenuation described in Section 4.1. Since we use a semi-spectral scheme the implementation was straightforward.

The scheme uses finite differences in the vertical direction, with 558 uniformly spaced grid points sampled at $\Delta z = 25$ km. In the horizontal direction we use a Fourier decomposition with 200 modes in the x direction and only 50 in the y. The spatial sampling is $\Delta x = 0.725$ Mm and $\Delta y = 1.45$ Mm. This seemingly low resolution is satisfactory because neither the initial wave-packet nor the sunspot

has any significant power at short-wavelengths. The size of the simulation box is 145 Mm long (x-coordinate), 72.5 Mm across (y-coordinate) and 14 Mm in depth (12.5 Mm below the photosphere). A typical run, such as the one from Section 5.3, takes approximately 14 days on a single CPU core.

4.3. Stabilizing the quiet-Sun atmosphere

Our aim is to model the propagation of waves through the solar atmosphere in such a way as to allow a direct comparison with the observations. The most direct way of proceeding would be to use an existing solar-like atmosphere such as that of model-S (Christensen-Dalsgaard et al., 1996). This most direct approach is however unavailable when considering the full evolution of wavepackets using numerical codes because both the solar and model-S atmospheres are convectively unstable.

Wave propagation through unstable atmospheres is difficult to study numerically because any numerical noise in the unstable modes grows exponentially and eventually dominates the numerical solution. The problem is then to stabilize the atmosphere whilst leaving it as solar-like as possible, at least in terms of the nature of the waves propagating through it.

The convective instability is easily understood by reference to equation (5). We imagine a small vertical displacement of a blob of plasma, and assume it is evolving slowly enough that it is in pressure balance with its surroundings. This implies $P' = 0$ and hence $c_0^2\rho' = \boldsymbol{\xi}\cdot\boldsymbol{\nabla}P_0 - c_0^2\boldsymbol{\xi}\cdot\boldsymbol{\nabla}\rho_0$. For a vertically stratified atmosphere this becomes $\rho' = \xi_z(\partial_z P_0 - c_0^2\partial_z\rho_0)/c_0^2$. The atmosphere is convectively unstable if an upward displacement ($\xi_z > 0$) corresponds to a region of lowered density ($\rho' < 0$); in such a case the fluid parcel is buoyant and accelerates upwards. The atmosphere is convectively stable when ξ_z and ρ' have the same sign, requiring $(\partial_z P_0 - c_0^2\partial_z\rho_0)/c_0^2 > 0$, equivalently

$$\partial_z P_0 > c_0^2\partial_z\rho_0. \tag{11}$$

We have the freedom to modify any combination of P_0, c_0 or ρ_0 in order to satisfy equation (11). It is somewhat natural to regard these three quantities as being related through an equation of state or through the constraint that the atmosphere be hydrostatic, however neither of these relationships is necessary in terms of the properties of the propagating waves. We choose P_0, c_0 and ρ_0 so that the wave speed is solar-like. Changing the sound speed would obviously have a major impact on the propagation of sound waves, and hence we have chosen to keep c_0 unchanged. Varying ρ_0 would have the effect of varying the distribution of the kinetic energy density of the different modes as a function of height, which would significantly change the sensitivity of wave packets to inhomogeneities; so we have also kept ρ_0 fixed. Thus we choose P_0 so that

$$\partial_z P_0 = \max\{0.9c_0^2\,\partial_z\rho_0,\ \partial_z P_{\rm u}\}, \tag{12}$$

where $P_{\rm u}$ was the pressure distribution of the unstable atmosphere. Notice that $\partial_z P_0$ is negative so that the factor of 0.9 does indeed mean that equation 11 is satisfied. The factor of 0.9 is possibly unnecessary, but does little harm: setting

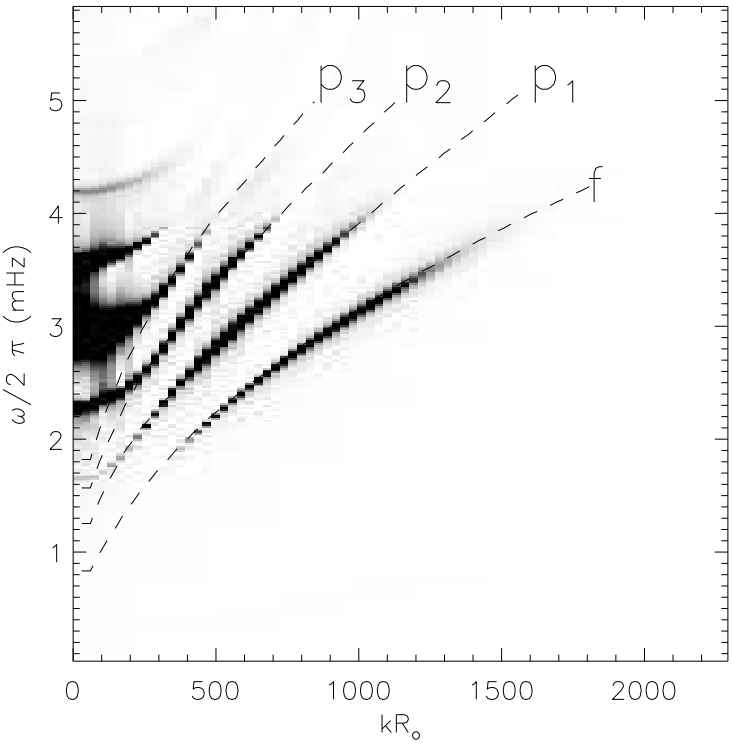

Figure 5. Power as a function of wavenumber and frequency for the example simulation described in Section 4.4 (no sunspot). The dashed lines correspond to the eigenfrequencies of the model-S atmosphere.

this factor to 1 should create stationary eigenmodes, setting it to 0.9 introduces internal gravity modes which propagate very slowly.

4.4. An example oscillation power spectrum

Since we have modified the atmosphere, we need to check whether it supports oscillations that are similar to those of the Sun and model S in the absence of a sunspot. We chose initial conditions consisting of a "line source" of the form

$$\xi_z = e^{-x^2/2s^2} e^{-(z-z_0)^2/2s^2} \quad \text{at } t = 0, \tag{13}$$

where $s = 0.7$ Mm and $z_0 = -250$ km is an arbitrary height below the photosphere. All other wave perturbations, ξ_x, ξ_y and $\boldsymbol{v}'$ being zero at $t = 0$. This disturbance encompasses many different modes allowing several ridges of the

dispersion diagram to emerge. Figure 5 directly compares these ridges with the eigenfrequencies of model S (A. C. Birch, private communication). The f modes and the acoustic modes p_1, p_2 and p_3 lie where they are expected for $kR_\odot > 300$. It is also to be noted that there is a very low amplitude ridge (not visible on the plot) at frequencies below 1 mHz that corresponds to internal gravity modes, which are not present in the Sun. They are an artifact of having made the system convectively stable as explained above, but they can be safely ignored.

The simulations and model-S eigenfrequencies differ strongly at wavenumbers less than $300/R_\odot$. This difference is due to the fact that our computational domain extends to only 12 Mm below the solar surface. We have not tested a deeper box because the f, p_1 and p_2 modes look satisfactory in the range of wavelengths we are interested in ($k > 300/R_\odot$).

4.5. A parametric sunspot model

In this section we will describe the sunspots we have embedded into our atmosphere. We begin by noting that we embed the sunspot into the atmosphere before we stabilize it in order to get the correct sound speed and density structures. We use $P_{\rm u}$ to denote the pressure of the atmosphere *before* it has been stabilized as described above. The sunspot is modeled by an axisymmetric magnetic field $\boldsymbol{B}_0 = \boldsymbol{B}_0(r, z)$, where r is the horizontal radial distance from the sunspot axis. Within the part of the atmosphere described by model-S, the magnetic field is made hydrostatic in a standard way, by calculating the Lorentz force $\boldsymbol{L} = (\boldsymbol{J}_0 \times \boldsymbol{B}_0)/4\pi$ and noting that the horizontal force balance then requires a horizontal pressure gradient $\partial_r P_{\rm u} = \hat{\boldsymbol{r}} \cdot \boldsymbol{L}$. Since $P_{\rm u}$ is unaffected by the spot at large distances, we can integrate from infinity towards the center of the spot to find P_0. Having thus found P_u we can find ρ_0 by the constraint of vertical force balance. In this case the gravitational force needs to balance both the vertical component of the Lorentz force as well as that of the pressure gradient. In principle given ρ_0 and P_0 the Saha equations need to be solved to obtain the first adiabatic exponent Γ_1 and the sound speed c_0. However for the purposes of this paper we have assumed that Γ_1 is a function of z only and is unaffected by the sunspot. This assumption will be relaxed in future studies.

The procedure thus outlined can always be applied, however in some cases the results will involve negative pressures or densities. Such solutions are of course unphysical and indicate that no hydrostatic solution exists for the given magnetic configuration and quiet-Sun pressure stratification. The problem typically arises in the very upper layers of the box when the magnetic pressure is large. For example a purely vertical flux tube with a magnetic pressure $P_{\rm m}$ cannot be in hydrostatic balance in an atmosphere with external pressure $P_{\rm ext} < P_{\rm m}$. In practice the Sun avoids such problems by rapidly evolving to almost force-free field configurations above the solar surface. The role of the Lorentz force in structuring the atmosphere in the low-beta region is thus artificial as well as being responsible for the lack of equilibrium. It is also dynamically of minor importance to the waves since it is above both the acoustic cut-off and the layer where the acoustic and Alfvén wave speeds become equal. We have therefore adopted the approach (Å. Nordlund, private communication) of scaling the Lorentz force in

this region when constructing the background atmosphere. The scaling factor was chosen to be $1/[1 + B_0^2/(8\pi P_{\rm qs})]$, where $P_{\rm qs}$ is the quiet-Sun pressure in the absence of the spot. This scaling factor works, although a more conservative scaling will be tested in the future.

Above the model-S atmosphere the density and pressure fall rapidly and hydrostatic balance requires an extreme scaling of the Lorentz force. However since we are not aiming to realistically model waves which reach these heights (we only want to damp them) this is not fatal. Instead of requiring a force balance in this purely artificial region we have chosen to put $P_0(x, y, z) = P_{\rm qs}(z)P_0(x, y, z_0)/P_{\rm qs}(z_0)$ where z_0 is the top of the model-S atmosphere and $P_{\rm qs}(z)$ is the pressure stratification of the system in the absence of the spot (the quiet Sun value). The density was similarly treated.

In this paper we follow Schlüter and Temesvary (1958), Deinzer (1965), and Schüssler and Rempel (2005) amongst others in concentrating on axisymmetric self-similar solutions. For this class of models, the vertical component of the magnetic field is assumed to satisfy

$$B_{0z}(r, z) = \mathcal{B}_0\, Q\left(r\sqrt{H(z)}\right)\, H(z), \tag{14}$$

where the functions Q and H satisfy $Q(0) = H(0) = 1$ but are otherwise arbitrary functions, and $\mathcal{B}_0$ is a scalar measure of the vertical field strength at the surface. The usual practice (Solanki, 2003), which we adopt in this paper, is to assume Q is a Gaussian,

$$Q(r) = e^{-(\ln 2)r^2/R_0^2}, \tag{15}$$

where R_0 is the half width at half maximum. We chose $R_0 = 10$ Mm to correspond to the observed value for sunspot AR9787, since R_0 is the half width at half maximum of the model sunspot at the surface. The value of R_0 is fixed throughout this paper. For the function H we chose the exponential function

$$H(z) = e^{z/\alpha}, \tag{16}$$

with $\alpha = 6.25$ Mm. This last choice is rather arbitrary and will certainly be varied in the near future. In this paper we concentrate on varying $\mathcal{B}_0$, the peak magnetic field at the surface. Having thus prescribed the formula for $B_{0z}(r, z)$ we determine $B_{0r}(r, z)$ by the requirement that $\boldsymbol{\nabla} \cdot \boldsymbol{B}_0 = 0$. Once we have such a hydrostatic solution we adjust the pressure everywhere to make it convectively stable in the manner described above.

5. Comparison between simulations and observations

In this section we want to compare the observed f-mode cross-covariance from AR 9787 and the simulations. The computational domain is -40 Mm$< x <$ 105 Mm, -36.25 Mm$< y <$ 36.25 Mm, and -12.5 Mm$< z <$ 1.5 Mm. The sunspot axis is $x = y = 0$. The relationship of the computational box to the observations is shown by the white rectangle in Figure 4.

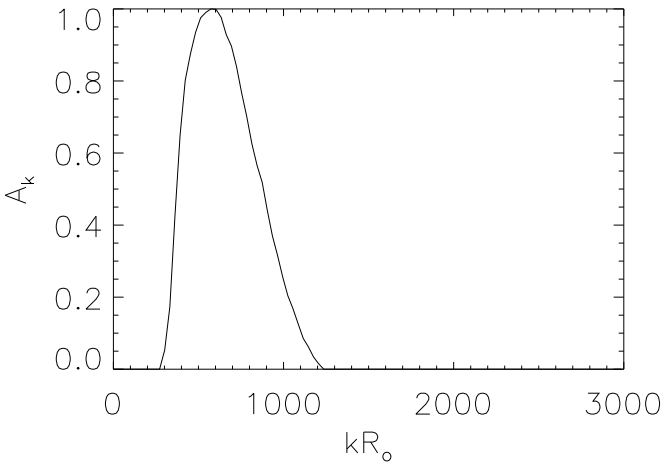

Figure 6. The initial distribution of f-mode amplitudes used in the simulations, A_k, as a function of $kR_\odot$.

5.1. The initial conditions for the simulation

In this section we discuss the choice of the initial conditions for the simulation. The aim is to allow a direct comparison between the simulated wave field (Section 4) and the observed cross-covariance function (Section 3). Since the observed cross-covariance uses the z component of the wave velocity as input data, we choose to use v'_z from the simulations for the comparison (this is also in accordance with a deeper interpretation of the cross-covariance, see Campillo, and Paul, A., 2003). The vertical component of velocity of any f-mode wave packet propagating in the $+\hat{\boldsymbol{x}}$ direction in a horizontally homogeneous atmosphere is of the form

$$v'_z(x,y,z,t) = \mathrm{Re}\sum_k A_k e^{kz} e^{\mathrm{i}k(x-x_0)-\mathrm{i}\omega_k t-\gamma_k t}, \tag{17}$$

where A_k are complex amplitudes, and $\exp(kz)$ and $\omega_k = \sqrt{gk}$ are the f-mode eigenfunction and eigenfrequency at wavenumber k. We introduced the reference coordinate $x_0 = -\Delta$, where $\Delta = 40$ Mm is defined in the previous section as the distance between Γ and the sunspot. Given the evolution equations (8) and (9), this wave packet is uniquely determined by the initial conditions

$$\boldsymbol{v}' = \mathrm{Re}\sum_k (\mathrm{i}\hat{\boldsymbol{x}} + \hat{\boldsymbol{z}})\, A_k e^{kz+\mathrm{i}k(x-x_0)}, \tag{18}$$

$$\boldsymbol{\xi} = \mathrm{Re}\sum_k (-\hat{\boldsymbol{x}} + \mathrm{i}\hat{\boldsymbol{z}})\, \omega_k^{-1} A_k e^{kz+\mathrm{i}k(x-x_0)}. \tag{19}$$

Thus our problem is reduced to fixing the amplitudes A_k. In this study, the amplitudes A_k are real (all waves are in phase at $x = x_0$ and $t = 0$) and are shown in Figure 6. This choice was simply the result of requiring that the simulated $v'_z(x, y, z = 0, t)$ and the cross-covariance look approximately the same, in the far field and in the absence of the sunspot. As will be shown in the next Section, this spectrum of wavenumbers is sufficiently accurate for the present study.

A more systematic analysis is planned. One important difficulty which arises is the existence of a background solar noise which is not easy to model and has been ignored in equation (17).

5.2. Magneto-acoustic waves

First we consider a sunspot model with $\mathcal{B}_0 = 3$ kG. The simulation enables us to understand what happens below the solar surface. The theory of the interaction of solar waves with sunspots had been developed using ray theory and two-dimensional numerical simulations (e.g. Cally, 2007; Bogdan et al., 1996). We find what appears to be very similar physics in our three-dimensional simulations: the strong "absorption" of the f modes is due to partial conversion of the incoming waves into slow magnetoacoustic waves which propagate along the field lines. This can be seen in Figure 7. The downward propagating slow magnetoacoustic modes experience a decrease in their speed as they propagate downwards and are therefore shifted to increasingly short wavelengths. Mode conversion is a very robust feature of this type of simulation. We note that the slow magnetoacoustic waves are much easier to see in x-component of wave velocity than in v'_z, which is why Figure 7 shows the former.

Since we are strongly damping short wavelengths these magneto-acoustic modes rapidly decay. Any upward propagating wave encounters the damping buffer situated above the photosphere and is also damped. In principle this decay is unphysical in both instances, however since neither the downward or upward propagating waves return to the surface this is not undesirable.

5.3. Wave forms

In this section we compare the simulated v'_z at $z = 0$ with the observed cross-covariance.

Figure 8 shows such a comparison between simulations and observations for times $t = 40$ min, $t = 100$ min and $t = 130$ min. The peak field strength used in this simulation was $\mathcal{B}_0 = 3$ kG and the radius $R_0 = 10$ Mm. The comparison appears to be very good at time $t = 130$ min, at which time the wavepacket has completely traversed the sunspot. At this time, all aspects of the waveform would appear to have been approximately reproduced by the simulation: amplitudes (including "absorption"), phases, and spatial spectrum. The match appears to be less good for $t = 40$ min; this will be discussed below.

To be more precise, however, the match between the simulations and observations must be better quantified. In order to reduce the observational noise, we have averaged the cross-covariance function in the y-direction over two bands. Both bands, shown in Figure 9, are 14.5 Mm wide in the y-direction. The bands

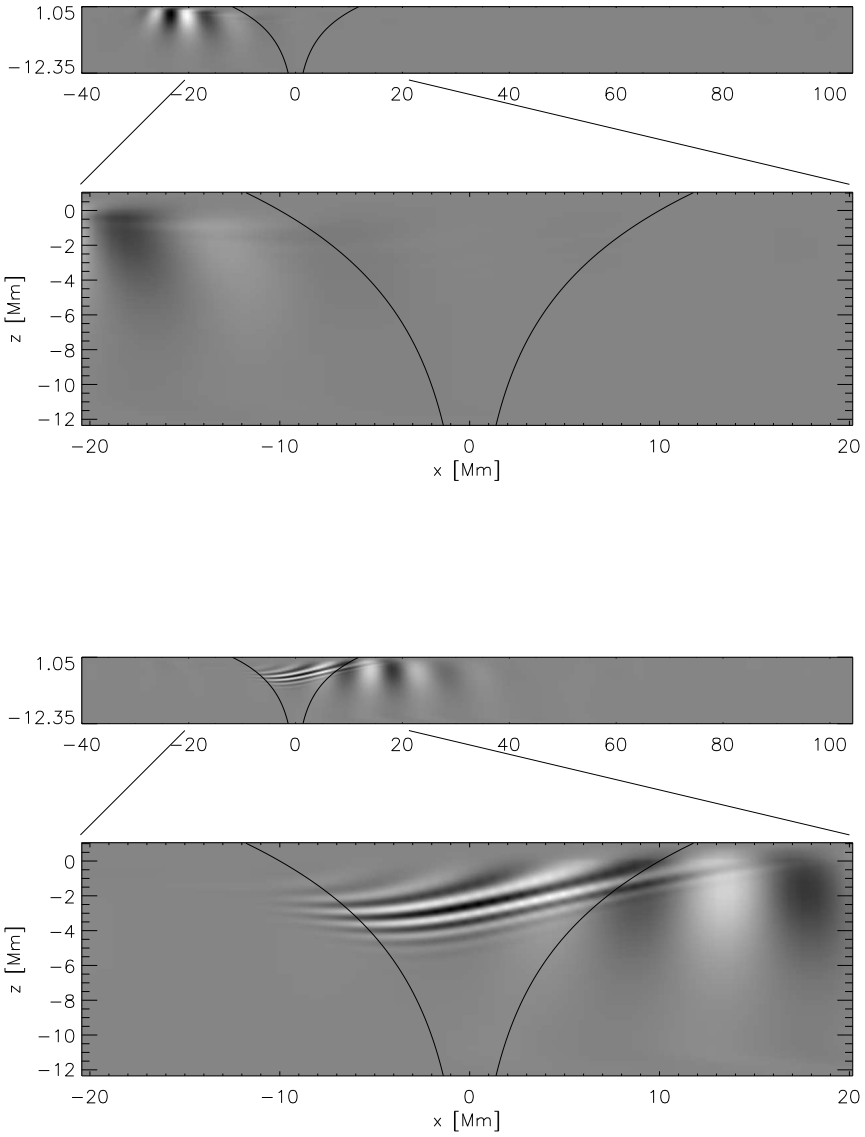

Figure 7. This plot shows $\rho_0 v_x'$ in the x—-z plane, through the sunspot axis. The upper frames are for time $t = 34$ min (before the f-mode wavepacket crosses the sunspot) and the lower frames are for $t = 84$ min (after). The black curves with equation $B_z(r, z) = B_z(r = 0, z)/2$ give an estimate of the "width" of the sunspot. The conversion of the incoming f modes into slow magnetoacoustic modes is evident in the lower frames.

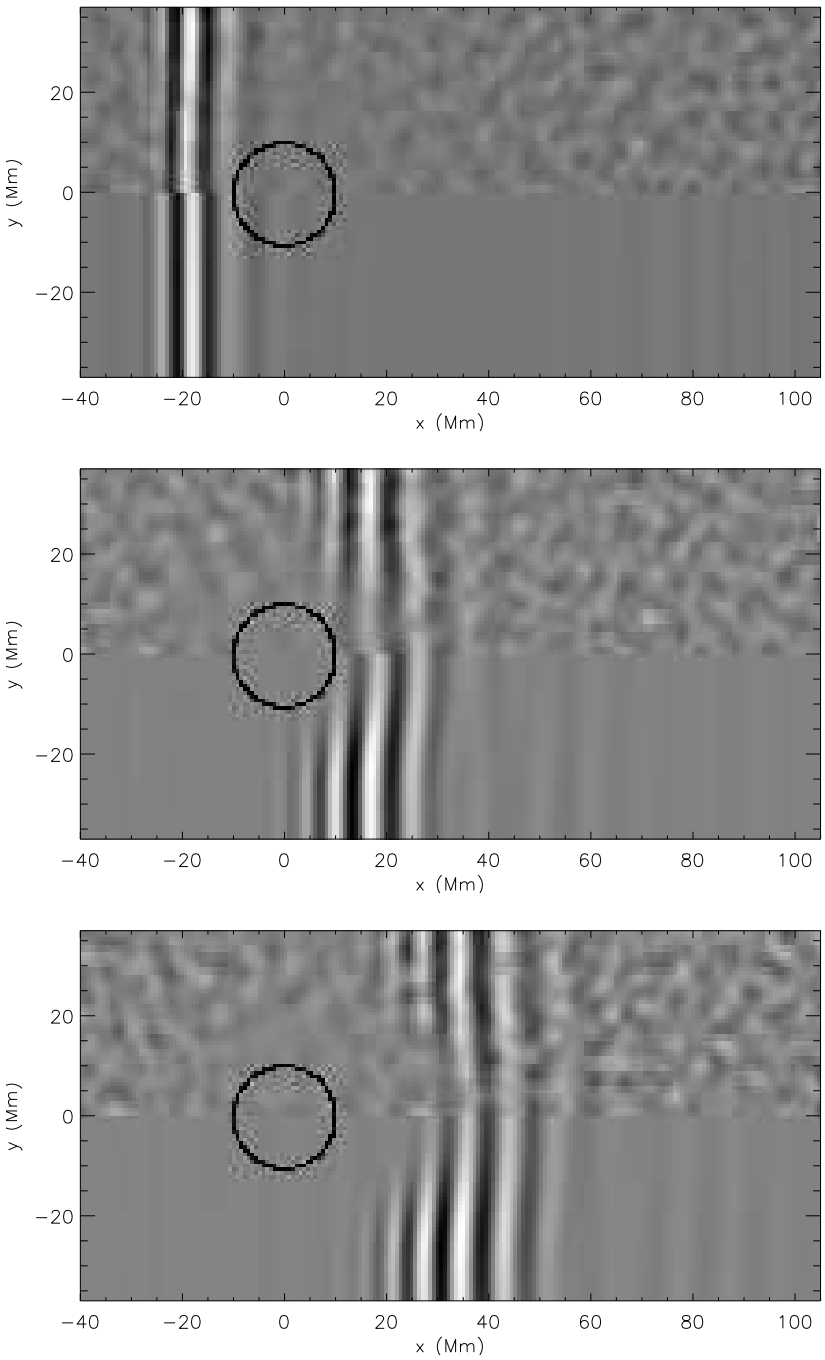

Figure 8. Comparison of the simulated vertical velocity and the observed cross-covariance. In each panel the upper frame shows the observed cross-covariance, the bottom panel the simulated wave packet. The panels correspond to $t = 40$ min, $t = 100$ min, and $t = 130$ min, from top to bottom. The black circles of radius $R_0 = 10$ Mm indicate the location of the sunspot.

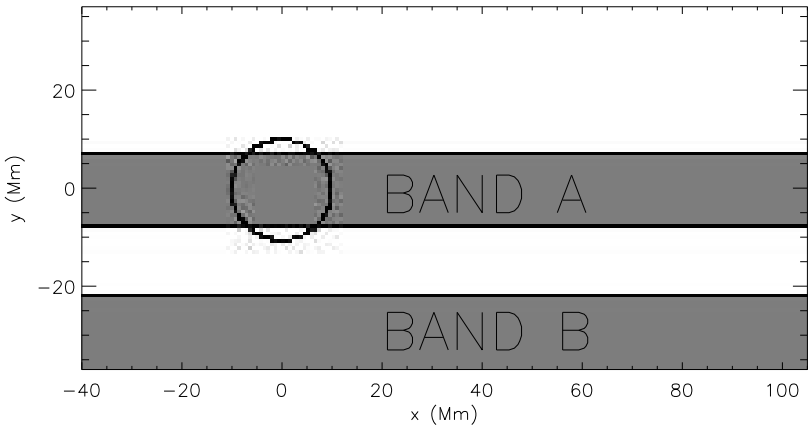

Figure 9. Sketch of the bands over which the data have been averaged in the y direction in later plots. Band A is centered on the spot, while band B acts as a reference.

are labeled A and B and centered around $y = 0$ and $y = \pm 29$ Mm. Band A is centered on the spot, while band B acts as a reference. The simulations are averaged in the same manner for comparison with the observations.

In Figure 10 we have plotted both the simulation (v_z', thick lines) and the observed cross-covariance (C, thin lines). In the top panels we compare the wave propagation at the edge of the computational box, i.e. in band B. This part of the wave is little affected by the sunspot and the match between the simulation and observation is quite good since the initial amplitude spectrum A_k was chosen accordingly. In the lower panels of Figure 10 we see the results for the waves passing through the spot, i.e. band A. First we notice that the wave amplitude is remarkably well reproduced in the simulations, meaning that mode conversion is the likely process by which the wave "absorption" is taking place. For $t = 130$ min, after the waves have crossed the sunspot, there is no appreciable phase shift between the simulation and the observations. The match, however, is somewhat worse at $t = 40$ min and there is an obvious phase shift between the two wave forms with the observations lagging behind the simulations. Given the value of the phase shift, we suspect that it is due to the effect of the moat flow. The moat flow is a horizontal outflow from the sunspot, which we have measured by tracking the small moving magnetic features. The observed moat velocity (averaged over 9 days) has a peak value of 230 m/s at a distance of 25 Mm from the center of the sunspot and vanishes at a distance of 45 Mm. The solar waves moving through the flow are first slowed down (against the flow) and

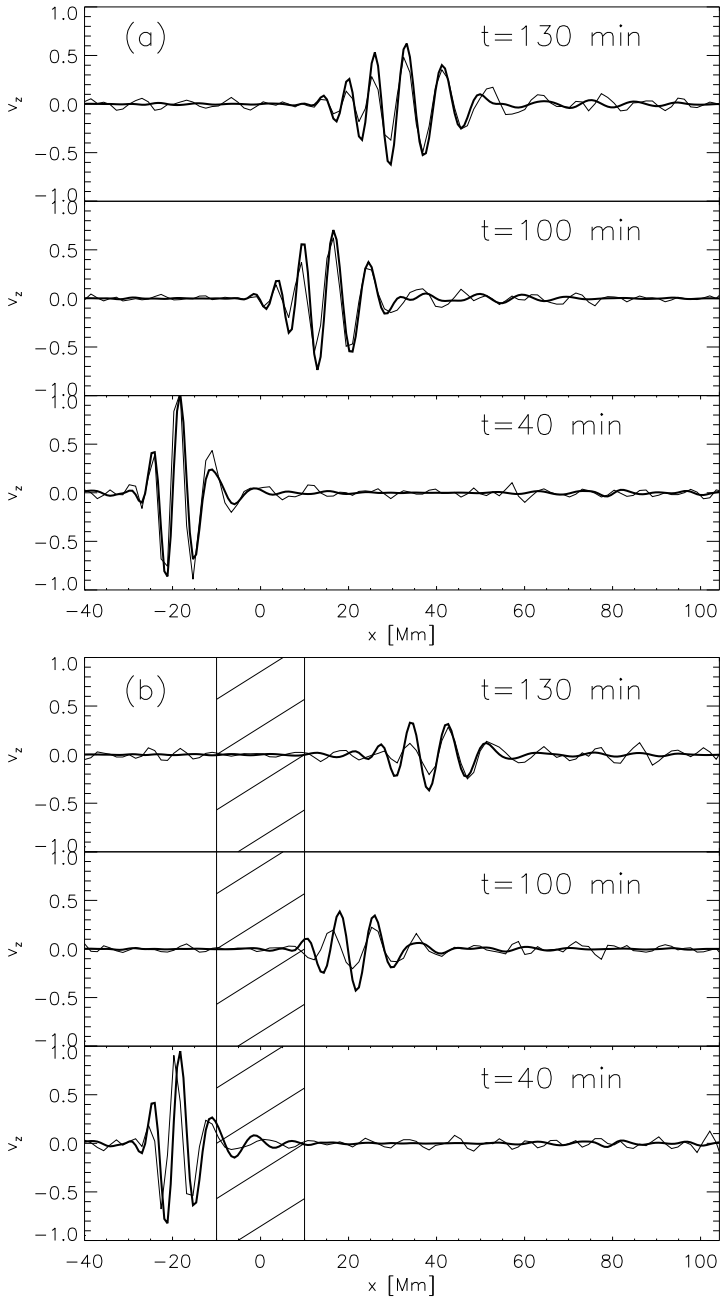

Figure 10. The top panels show the simulation (v'_z, thick lines) and the observed cross-covariance (C, thin lines) averaged in the y-direction across band B (reference), at three different times t. The bottom panels show the simulation (v'_z, $\mathcal{B}_0$ = 3 kG, thick lines) and observed cross-covariance (C, thin lines) averaged in the y-direction across band A, at three different times t. The effect of the sunspot is very easily seen, by comparing with band B.

later sped up again (with the flow). This effect we have not modeled yet. It is reassuring, however, to see that the Doppler shift caused by the moat appears to have disappeared at $t = 130$ min.

Reiterating, it appears that, by using numerical simulations, seismic signatures can be followed through their passage across the spot.

6. Constraining B

The solutions shown thus far have been for a model sunspot with a peak vertical field strength $\mathcal{B}_0 = 3$ kG at the surface $z = 0$. The match is good which raises the question of whether other field strengths would match as well. The answer to this question can be seen in Figures 11 where we show the comparison between the simulations and observations for different field strengths, $\mathcal{B}_0 = 2$ kG and $\mathcal{B}_0 = 2.5$ kG. The comparison is made some time after the wave packet has passed through the sunspot, so the issue of the moat flow does not arise. At this stage we restrict ourselves to commenting that qualitatively the match is best, in phase and amplitude, for $\mathcal{B}_0 = 3$ kG; for the other values of $\mathcal{B}_0$ there is an apparent phase mismatch along $y = 0$ and the amplitude of that part of the wave passing through the spot is not sufficiently damped. The quantification of the "goodness of fit" between the simulation and observations, which will allow a more accurate determination of the field strength, will be the subject of a future study.

7. Discussion

We have performed three-dimensional MHD simulations of waves propagating through sunspot models and have compared the results with observed cross-covariances. The parameters of the sunspot model can be chosen in such a way that its helioseismic signature is in good agreement with helioseismic observations of sunspot AR9787. A qualitative study using f modes has enabled us to place a constraint, $\mathcal{B}_0 \geq 3$ kG, on the sunspot's near-surface field strength. The remaining differences reflect real differences between the model and the observed sunspot, such as the moat flow.

The model atmosphere that we have constructed also supports p modes with a dispersion relation which is very close to that of the Sun. Obviously, the p modes in combination with the f modes should enable us to place more substantial constraints on the subsurface structure of the sunspot. In particular, it should be possible to simultaneously constrain the magnetic field strength $\mathcal{B}_0$, the sunspot radius R_0, and the magnetic field inclination (controlled by the parameter α). Of course, the parametric sunspot model that we have considered in this paper is just one particular model: we plan to consider other types of sunspot models in the future.

In summary, we believe that we have shown that the full-waveform modeling of sunspots is feasible.

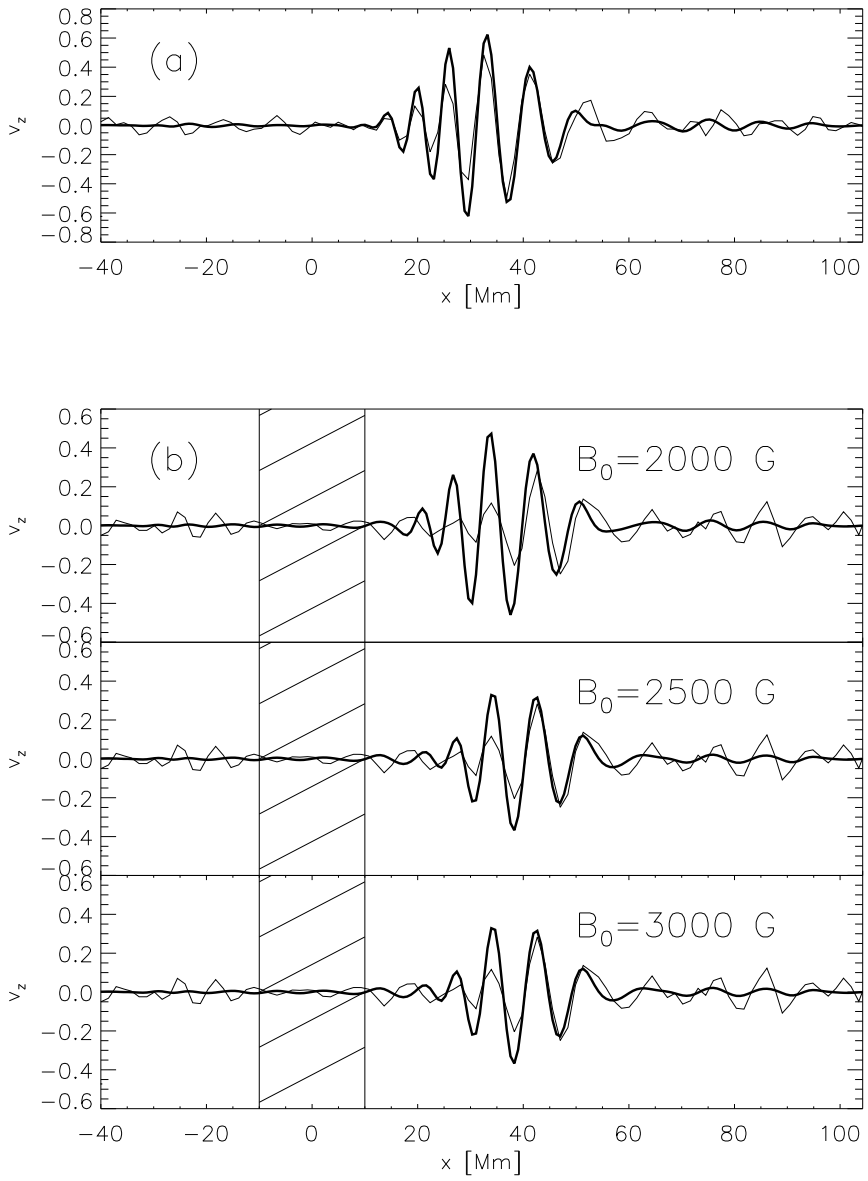

Figure 11. Simulated vertical velocity (thick lines) and observed cross-covariance (thin lines) at $t = 130$ min. (a) For the band at the edge of the domain (large y). (b) For the band passing through the sunspot ($y = 0$). The three panels correspond to simulations using is $\mathcal{B}_0 = 2$ kG, 2.5 kG and 3 kG. It is seen that the simulations with $\mathcal{B}_0 = 3$ kG provide the best match in terms of both amplitude and phase. The stripes indicate the location of the sunspot.

Acknowledgements SOHO is a project of international collaboration between ESA and NASA. We are grateful to Manfred Schüssler for insightful discussions.

References

Bogdan, T. J., Hindman, B. W., Cally, P. S., and Charbonneau, P.: 1996, *Astrophys. J.* **465**, 406.
Braun, D. C.: 1995, *Astrophys. J.* **451**, 859.
Braun, D. C. and Lindsey, C.: 2000, *Solar Phys.* **192**, 285.
Cally, P. and Bogdan, T.: 1997, *Astrophys. J.* **486**, L67.
Cally, P.: 2007, *Astron. Nachr.* **328**, 286.
Cameron, R., Gizon, L., and Daiffallah, K.: 2007, *Astrophys. Nachr.* **328** 313.
Campillo, M., and Paul, A.: 2003, *Science* **299**, 547.
Colin de Verdière, Y.: 2006, http://fr.arxiv.org/abs/math-ph/0610043/.
Christensen-Dalsgaard, J., Däppen, W., Ajukov, S. V., Anderson, E. R., Antia, H. M., Basu, S., Baturin, V. A., Berthomieu, G., Chaboyer, B., Chitre, S. M., Cox, A. N., Demarque, P., Donatowicz, J., Dziembowski, W. A., Gabriel, M., Gough, D. O., Guenther, D. B., Guzik, J. A., Harvey, J. W., Hill, F., Houdek, G., Iglesias, C. A., Kosovichev, A. G., Leibacher, J. W., Morel, P., Proffitt, C. R., Provost, J., Reiter, J., Rhodes Jr., E. J., Rogers, F. J., Roxburgh, I. W., Thompson, M. J., Ulrich, R. K.: 1996, *Science* **272**, 1286.
Couvidat, S., Birch, A. C., and Kosovichev, A. G.,: 2006 *Astrophys. J.* **640**, 516.
Crouch, A. D., Cally, P. S., Charbonneau, P., Braun, D. C., and Desjardins, M.: 2005, *Mon. Not. R. Astron. Soc.* **363**, 1188.
Deinzer, W.: 1965, *ApJ* **141**, 548.
Duvall, T. L., Jefferies, S. M., Harvey, J. W., and Pomerantz, M. A.: 1993, *Nature* **362**, 430.
Duvall, T. L., Kosovichev, A. G., and Murawski, K.: 1998, *Astrophys. J.* **505**, L55
Gizon, L. and Birch, A. C.: 2002, *Astrophys. J.* **571**, 966.
Gouédard, P., Stehly, L., Brenguier, F., Campillo, M., Colin de Verdière, Y., Larose, E., Margerin, L., Roux, Ph., Sánchez-Sesma, F. J., Shapiro, N., Weaver, R.: 2007, Geophysical Prospecting, accepted.
Kosovichev, A. G., Duvall, T. L., and Scherrer, P. H.: 2000, *Solar Phys.* **192**, 159.
Lindsey, C. and Braun, D. C.: 1997, *Astrophys. J.* **485**, 895.
Parker, E.: 1979, *Astrophys. J.* **230**, 905.
Schüssler, M. and Rempel, M.: 2005, *Astron. Astrophys.* **441**, 337.
Schlüter, A. and Temesvary, S.: 1958, in *Electromagnetic phenomena in cosmical physics, IAU Symp.* **6**, 263.
Solanki, S.: 2003, *Astron. Astrophys. Rev.* **11**, 153.
Zhao, J., Kosovichev, A. G., and Duvall, T. L.: 2001, *Astrophys. J.* **557**, 384.